Supporting Information

Non-linear optics at twist interfaces in h-BN/SiC heterostructures

Abhijit Biswas, Rui Xu, Gustavo A. Alvarez, Jin Zhang*, Joyce Christiansen-Salameh, Anand B. Puthirath, Kory Burns, Jordan A. Hachtel, Tao Li, Sathvik Ajay Iyengar, Tia Gray, Chenxi Li, Xiang Zhang, Harikishan Kannan, Jacob Elkins, Tymofii S. Pieshkov, Robert Vajtai, A. Glen Birdwell, Mahesh R. Neupane, Elias J. Garratt, Tony G. Ivanov, Bradford B. Pate, Yuji Zhao, Hanyu Zhu*, Zhiting Tian*, Angel Rubio*, and Pulickel M. Ajayan**

Abhijit Biswas, Rui Xu, Gustavo A. Alvarez, Jin Zhang equally contributed to this work

Keywords: h-BN films, nano-domains, twist-interfaces, second harmonic generation, thermal conductivity, time dependent density functional theory

E-mails: **abhijit.biswas@rice.edu, jin.zhang@mpsd.mpg.de, hanyu.zhu@rice.edu, zhiting@cornell.edu, angel.rubio@mpsd.mpg.de, ajayan@rice.edu**

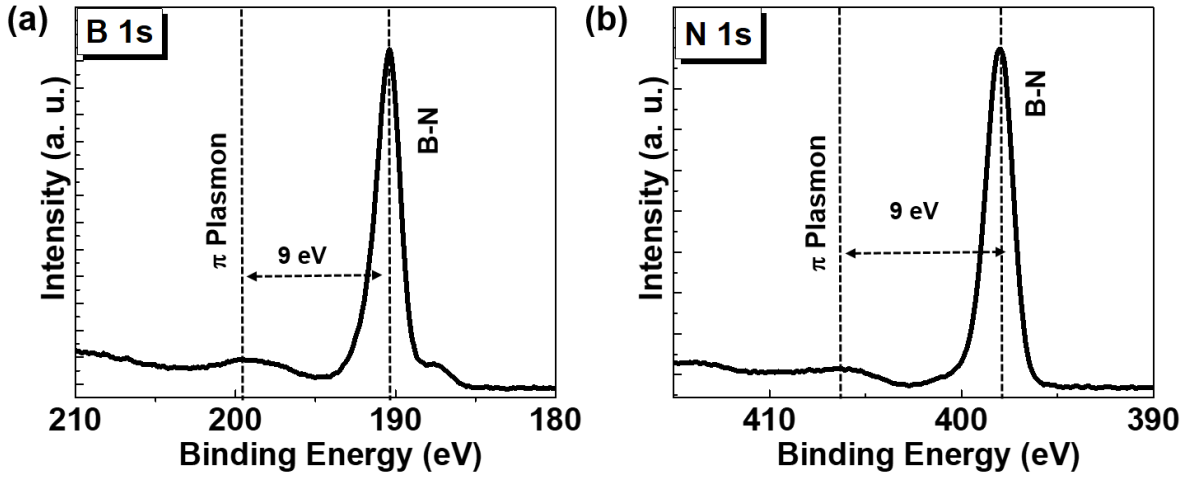

Figure S1: Structural characterizations of a 10 nm h-BN film. (a), (b) B 1s core and N 1s core X-ray photoelectron spectroscopy shows the characteristics of B-N peaks.

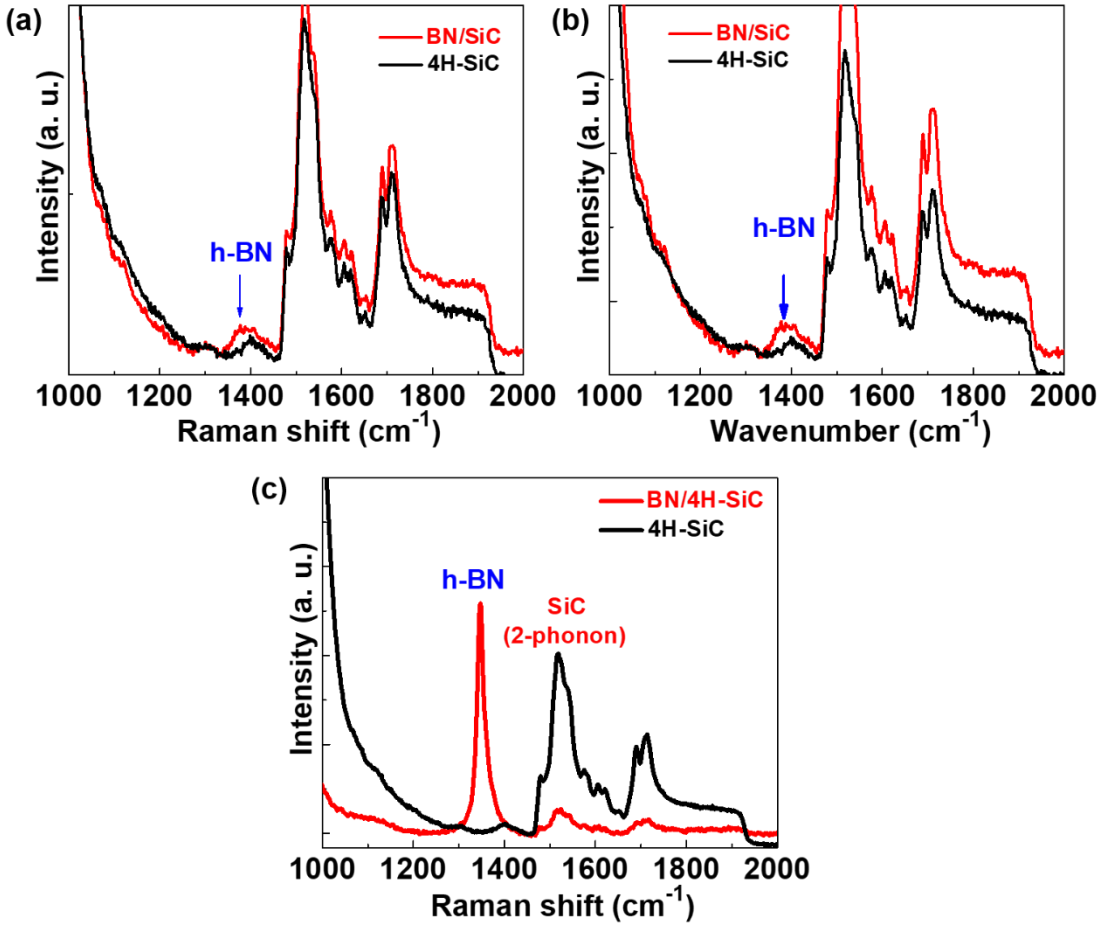

Figure S2: (a), (b) Raman spectra at several places of a thin h-BN film showing a hump around ~1360-1380 cm^{-1}, corresponding to the transverse optical E_{2g} vibrations for in-plane B-N bond stretching in sp^2 bonded h-BN. (c) Raman spectra of a thick 300 nm BN/SiC film shows a clear E_{2g} h-BN peak.

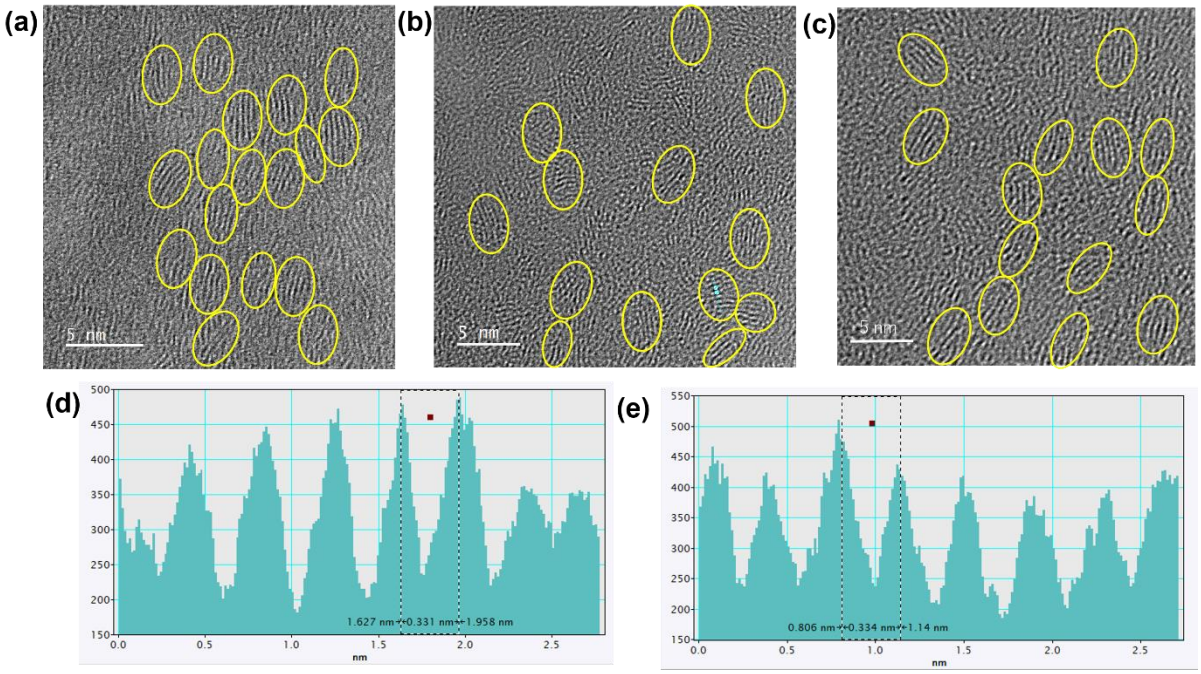

Figure S3: (a)-(e) Several nano-domain regions with clear crystalline fringes (*d*-spacing of ~0.33 nm) are also observed, corresponding to interplanar *d*-spacing of (0002) h-BN.

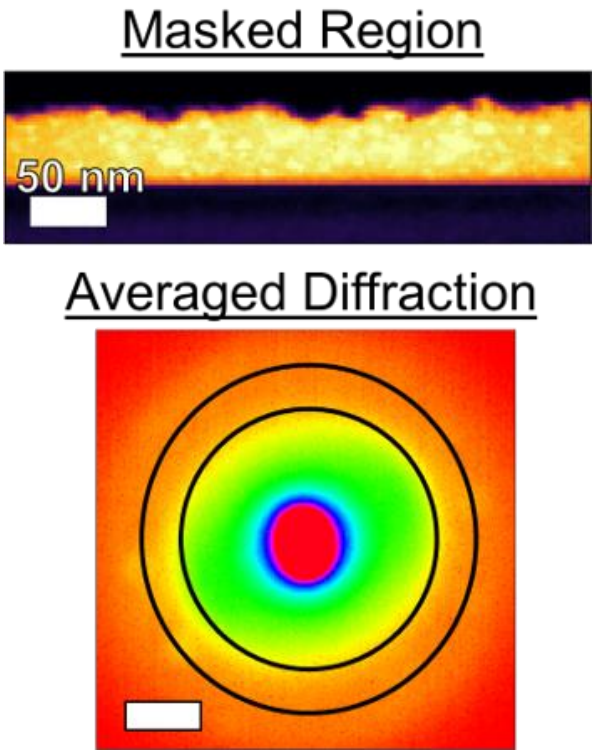

Figure S4: 4D-STEM analysis. The BN film is masked here so that the SiC and Au are omitted from visualizing the diffraction pattern. Mean diffraction from the different regions in the BN film. Weakly diffracted Bragg disks can be seen from the localized crystallites in the film. Scale bar is 5 mrad.

.

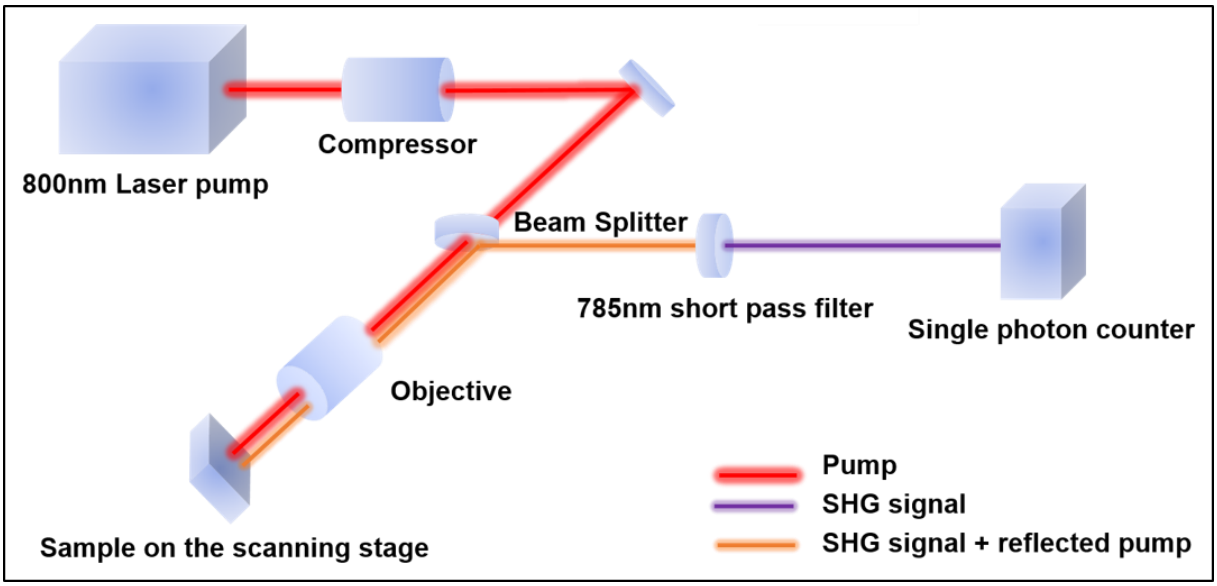

Figure S5: Schematic of the second harmonic generation (SHG) excitation and collection from the h-BN film surface.

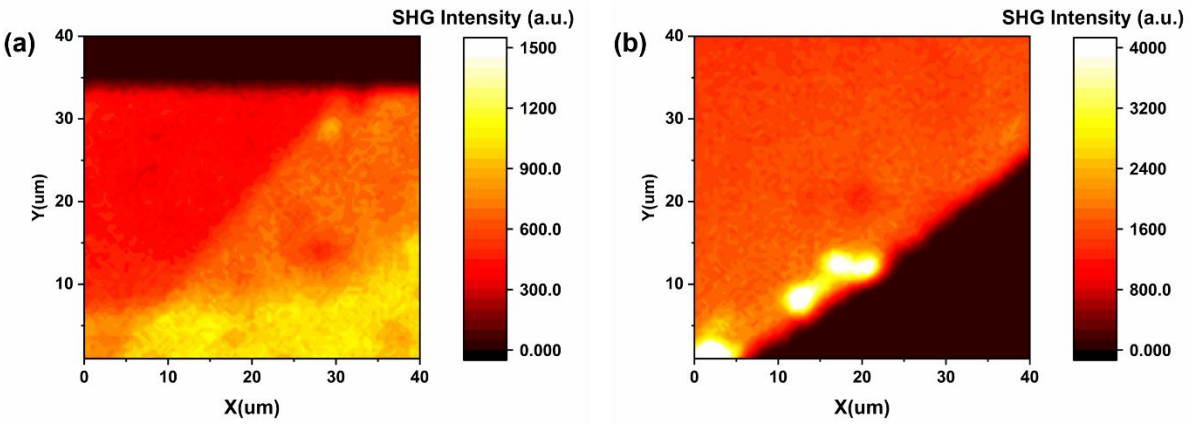

Figure S6: (a), (b) Spatial SHG intensity mapping of 30 nm (left) and 50 nm (right) h-BN films.

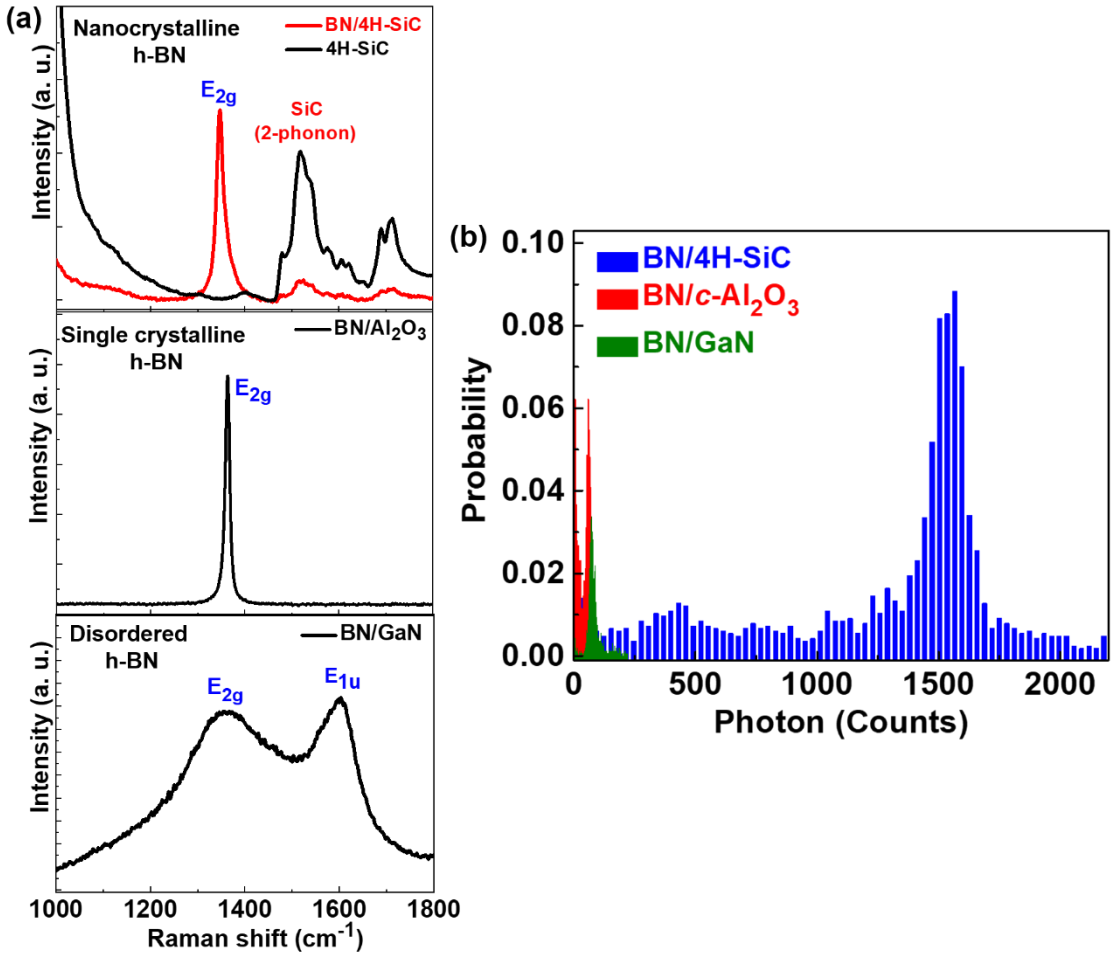

Figure S7: (a) Raman spectra, and (b) SHG response of h-BN thin films grown on SiC, *c*-Al_2O_3 and GaN substrates showing much stronger SHG signal for BN/SiC.

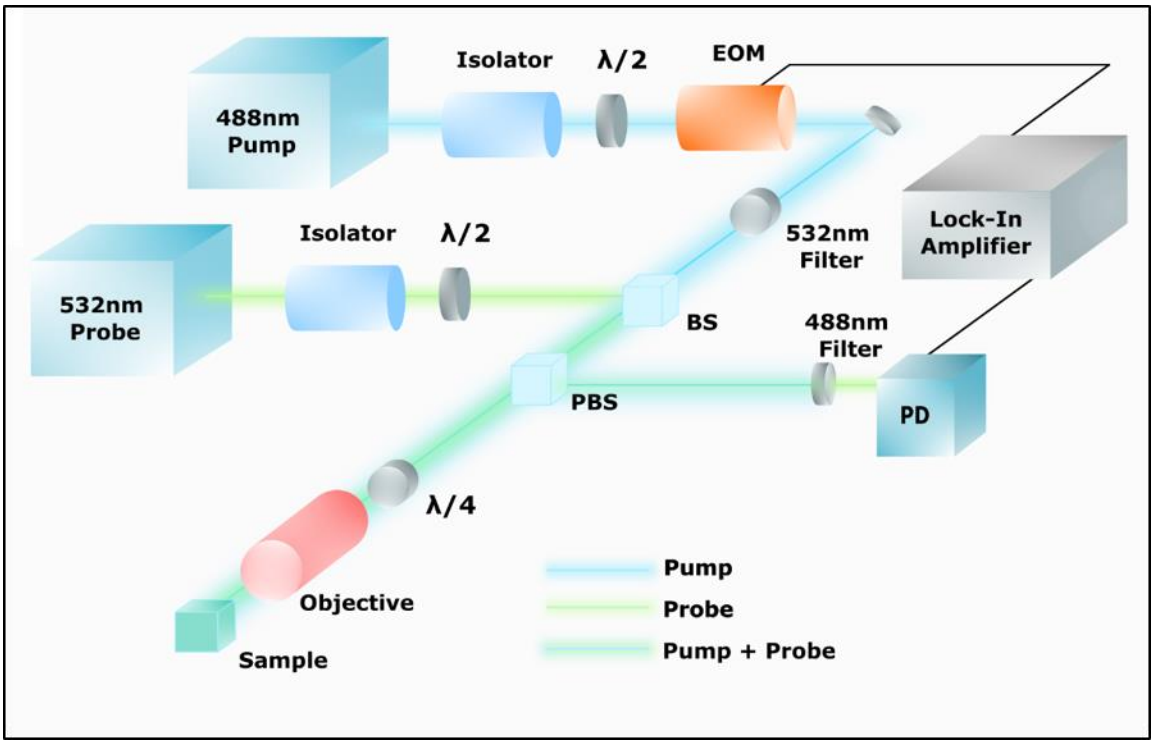

Figure S8: Schematic of the FDTR setup for the thermal conductivity measurement.

Frequency-domain thermoreflectance (FDTR) details:

The detailed derivation of the mathematical model can be found elsewhere.[51,71] The phase lag of the probe beam, measured with respect to the reference signal from the lock-in amplifier, is compared against the calculated phase lag of the sample surface temperature to a periodic Gaussian heat source at the sample surface.[51] Mathematically, the solution to the calculated phase lag (based on individual materials physical properties of interest, in our case k and G_2) can be expressed as a complex number Z(ω_o), such that the output of the lock-in amplifier for a reference wave $e^{i\omega_o t}$ is given by

$$Ae^{i(\omega_o t+\phi)} = Z(\omega_o)e^{i\omega_o t} \tag{S1}$$

where ω_o is the modulation frequency, A is the amplitude, and ϕ the phase of the fundamental component of the probe signal with respect to the reference wave.[51]
In the case of continuous-wave pump and probe beams

$$Z(\omega_o) = \beta H(\omega_o) \tag{S2}$$

where β is a factor including the thermoreflectance coefficient of the sample and the power of the pump and probe beams.[51] $H(\omega_o)$ is the thermal frequency response of the sample weighted by the intensity of the probe beam.[51] The weighted sample frequency response, $H(\omega_0)$, is obtained by solving the heat diffusion equation for a Gaussian heat source (the pump beam) impinging on a multilayer stack of materials and weighting the resulting temperature distribution at the top surface by the Gaussian intensity distribution of the probe beam.[51]

As an example, for a single slab of material in the frequency domain, the temperature θ_t and the heat flux f_t on the top side of the slab are related to the temperature θ_b and the heat flux f_b on the bottom side through

$$\begin{bmatrix}\theta_b \\ f_b\end{bmatrix} = \begin{bmatrix}\cosh(qd) & \frac{-1}{k_\perp q}\sinh(qd) \\ -k_\perp q\sinh(qd) & \cosh(qd)\end{bmatrix}\begin{bmatrix}\theta_t \\ f_t\end{bmatrix} \tag{S3}$$

where d is the layer thickness, $k_\perp$ the cross-plane thermal conductivity and

$$q^2 = \frac{k_{\parallel}\mathcal{H}^2 + \rho c i\omega}{k_{\perp}} \tag{S4}$$

where $\mathcal{H}$ is the Hankel transfer variable, ρ is the density, c is the specific heat capacity, and $k_{\parallel}$ is the radial thermal conductivity.[2] The heat flux boundary condition at the top layer f_t is given by the Hankel transform of a Gaussian spot with power A_o and $1/e^2$ radius of the pump beam on the surface w_0

$$f_t = \frac{A_0}{2\pi} exp\left(\frac{-\mathcal{H}^2 w_0^2}{8}\right) \tag{S5}$$

Multiple layers are handled by multiplying the matrices for individual layers together

$$\begin{bmatrix}\theta_b \\ f_b\end{bmatrix} = \boldsymbol{M}_n \boldsymbol{M}_{n-1} \dots \boldsymbol{M}_1 = \begin{bmatrix}A & B \\ C & D\end{bmatrix}\begin{bmatrix}\theta_t \\ f_t\end{bmatrix} \tag{S6}$$

where $\boldsymbol{M}_n$ is the matrix for the bottom layer.[51] An interface conductance G is treated by taking the limit as the heat capacity of a layer approaches zero and choosing $k_{\perp}$ and d such that $G = k_{\perp}/d$. Since we treat the nth layer as semi-infinite, Eq. (S5) reduces to

$$\theta_t = \frac{-D}{C} f_t \tag{S7}$$

The final frequency $H(\omega)$ in real space is found by taking the inverse Hankel of Eq. (S6) and weighting the results by the probe intensity distribution, which is taken as a Gaussian spot with $1/e^2$ radius of the probe beam on the surface w_1

$$H(\omega_0) = \frac{A_0}{2\pi}\int_0^{\infty} \mathcal{H}\left(\frac{-D}{C}\right) \exp\left[\frac{-\mathcal{H}^2(w_0^2 + w_1^2)}{8}\right] d\mathcal{H} \tag{S8}$$

This result is inserted into Eq. (S2), where the measurement of individual materials physical properties is performed as an inverse problem, minimizing the error between the lock-in phase data and the phase of Eq. (S2) via a non-linear least-squares algorithm.[51] Phase vs frequency data for each of the three spot measurments on the sample are shown below (**Figure S9**).

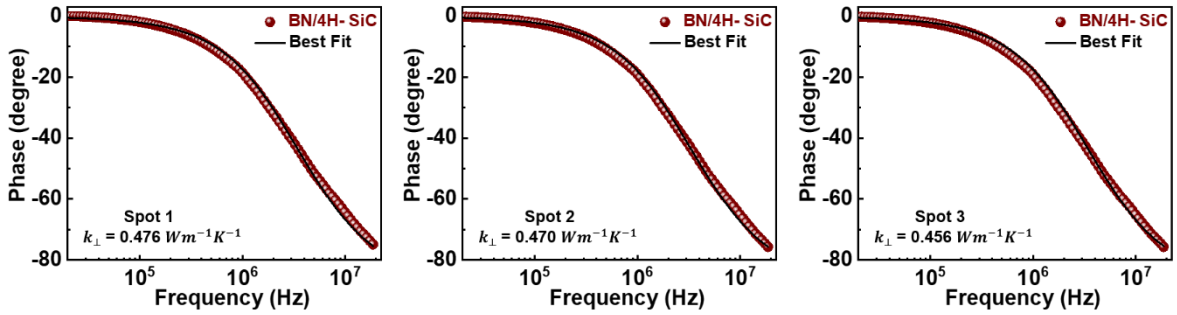

Figure S9: Phase vs. frequency data obtained from FDTR measurements shows a good approximation to the calculated best-fit curve. Each measurement is an average of three runs on three separate spots on the sample (i.e. nine measurements in total).

Sensitivity Analysis:

The sensitivity of the phase signal, S_x, to a parameter x is determined by

$$S_x = \frac{\partial \phi}{\partial lnx} \tag{S9}$$

where ϕ is the phase in radians, expressed as

$$\phi = \tan^{-1}\frac{\Im(H(\omega))}{\Re(H(\omega))} \tag{S10}$$

where ω is the modulation frequency and H is the final frequency response of Eq. (S8). Eq. (S9) is evaluated for the thermal conductivity $k_\perp$ of the Au transducer layer, the thermal boundary conductance G_1 and G_2, and the $k_\perp$ of h-BN.

Uncertainty Analysis:

We used the analytical method to estimate the uncertainty of our fitted data based on the parameters and measurement.[52] We assumed uncertainty of 3% for the volumetric heat capacity,[52] and 4% for the thicknesses of the Au transducer layer and h-BN epilayer. To explore uncertainties of multiple unknown parameters, Jacobian matrices were used in the calculation. We selected the analytical method because it accumulates uncertainties from the parameters and measurements in the Jacobian matrices. The consideration of correlation would not overestimate the uncertainty.[72] Given the measured signal Φ and known parameter matrix X_C, the variance-covariance matrix of unknown matrix X_U is

$$var(X_U) = (J_U'J_U)^{-1}J_U'(var(\Phi) + J_C var(X_C)J_C^{-1})J_U(J_U'J_U)^{-1} \tag{S11}$$

Here, $var(\Phi)$ and $var(X_C)$ are the diagonal matrices whose elements are variances of measured signal and known parameters, respectively.[50] J_C and J_U are the Jacobian matrices of known and unknown parameters accordingly with the form:

$$J = \begin{pmatrix} \frac{\partial f(\omega_1, X)}{\partial x_1}|X^* & \cdots & \frac{\partial f(\omega_1, X)}{\partial x_N}|X^* \\ \vdots & \ddots & \vdots \\ \frac{\partial f(\omega_M, X)}{\partial x_1}|X^* & \cdots & \frac{\partial f(\omega_M, X)}{\partial x_N}|X^* \end{pmatrix} \quad \text{(S12)}$$

where $f(\omega_M, X)$ is the function to calculate the phase lag between pump and probe signals, ω_i, $i = 1, \cdots, M$ are the frequency that takes the measurement, x_j, $j = 1, \cdots, N$ are the parameters and X^* is the matrix of the fitted data.[52] The diagonal elements of $var(X_U)$ are the variances of the unknown parameters. Thus, this analysis consists of the propagation of errors and the variance among different measurement spots (i.e., the standard error of the six different spot locations, which is incorporated in $var(\Phi)$).

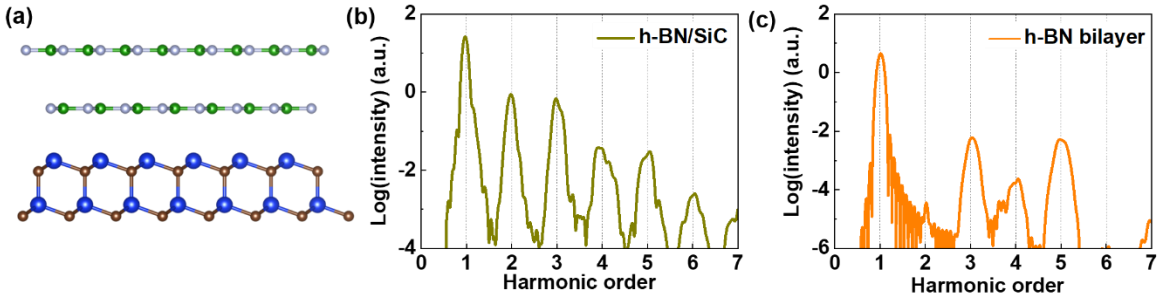

Figure S10: Theoretical insights for the high harmonic generation from twisted h-BN/SiC layers. (a) Atomic structures of the BN/SiC heterostructure. Top: h-BN bilayer with AA' stacking order and bottom: 4H-SiC slab. (b) High harmonic spectrum for the h-BN/SiC heterostructure. (c) High harmonic spectrum for h-BN bilayer.

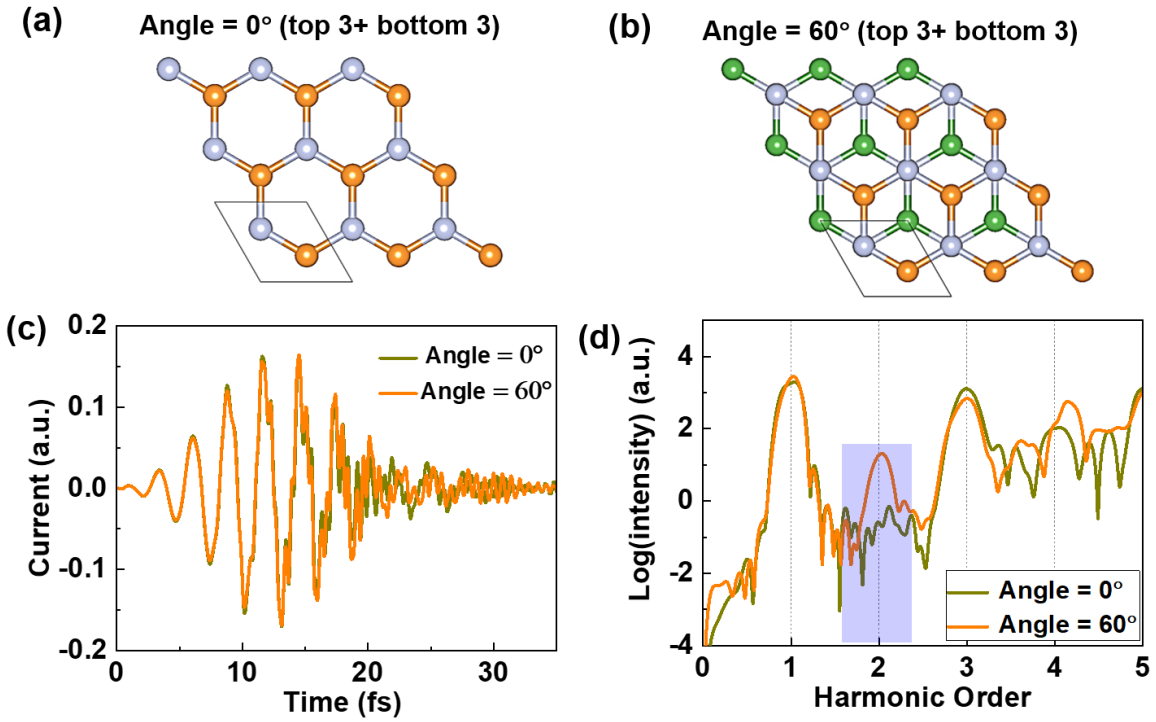

Figure S11. Laser-induced total currents and corresponding high harmonic spectra in h-BN. (a),(b) Atomic structures for the two-twisted angle. (c) Time-dependent electronic current for bulk h-BN, computed with different angles. (d) Higher harmonic spectra for h-BN layers with twist angles of 0°and 60°, respectively, highlights the strength of second harmonics. For the twist angle of 21.79°, the laser-induced total current is not applicable to compare directly with the twist angles of ~0°and 60° because the supercell changes the total numbers of atoms and electrons.